Quantum-classical correspondence in entanglement production: Entropy and classical tori

Shi-hui Zhang and Quan-lin Jie

Department of Physics, Wuhan University, Wuhan 430072, P. R. China

(Received 23 June 2007; published 14 January 2008)

We analyze the connections between entanglement dynamics and classical trajectories in a semiclassical regime for two systems: A pair of coupled oscillators and the Jaynes-Cummings model. We find that entanglement production depends on classical invariant tori and such phenomenon is closely related to the power spectra of classical trajectories. Classical power spectrum with a larger number of frequency components corresponds to larger entanglement. We introduce a frequency entropy to describe the classical frequency distribution. It is found that there is good correspondence between the classical frequency entropies and the maximum von Neumann entropies.

I. INTRODUCTION

Problems of quantum-classical correspondence have been extensively investigated [1]. Recent studies have further shown the relations between entanglement production and the underlying classical dynamics for chaotic systems. In the early works on spin-boson system [2] and coupled kicked tops [3], it was suggested that entanglement production can be a good indicator of the regular to chaotic transition for classical chaotic systems. This claim has been affirmed in many subsequent studies [4–6]. Also it has been revised in some recent works [7–9]. An investigation on a pair of coupled kicked tops showed that increased chaos corresponds to a saturation of entanglement production rate in the weakly coupled regime [7]. Another study on Rydberg molecules [8] found that the quantum-classical correspondence in entanglement production is related to the inelastic scattering. Especially, a semiclassical approach shown by Jacquod [9] concluded that the entanglement production in bipartite system depends on both the degree of chaos and the coupling strength.

The aim of this paper is to further explore the connections between entanglement production and the underlying classical trajectories in a semiclassical regime for chaotic systems. In Sec. II, we investigate the dependence of entanglement production on the classical trajectories for the two coupled oscillators. We find that the production of entanglement is strongly related to the classical trajectories. The maximum values and rates of entanglement production correspond systematically to the classical invariant tori. When the initial state lies at the edge of regular islands for the regular case or in the chaotic sea for the mixed case, the production of entanglement is maximized.

Furthermore, the above correspondences between the production of entanglement and the classical trajectories are closely related to the classical power spectrum. The more complicated classical power spectra correspond to the larger maximum values and rates of entanglement production. We thus define a frequency entropy to measure the frequency distribution of classical power spectrum. It is shown that there is a good correspondence between the frequency entropies and the maximum von Neumann entropies for different classical trajectories (especially for regular ones). Such cor-

respondence is also found in the investigations on the Jaynes-Cumming model presented in Sec. III. This is because a classical power spectrum reveals the structure of the energy levels involved in the quantum evolution [10–12]. The latter is directly connected to the entanglement production [13]. Thus the classical power spectrum and the classical frequency entropy can indicate the behavior of entanglement production.

II. ENTANGLEMENT PRODUCTION IN A BIPARTITE MODEL

We now study the entanglement of a bipartite system with a model of two coupled oscillators, which is often used to analyze decoherence [14] or construct qubit models [15,16]. The Hamiltonian reads

$$H = \frac{p_1^2}{2m} + \frac{p_2^2}{2m} + \frac{1}{2}m\omega^2 q_1^2 + \frac{1}{2}m\omega_2^2 + \lambda q_1^2 q_2^2, \qquad (1)$$

where m and ω are the mass and frequency of any of the two oscillators. λ is the coupling parameter. This system is proposed by Pullen and Edmonds [17] and used in many works to study the classical-quantum correspondence for chaotic systems [18].

In this section, using the model (1), we investigate the entanglement dynamics in both the regular and mixed cases to achieve a detailed picture of the relations between the entanglement production and the classical trajectories. In the calculations, we adopt the natural units for the harmonic oscillator, i.e., $\hbar\omega$ for energy, $\sqrt{\hbar/m\omega}$ for length and $\sqrt{\hbar m\omega}$ for momentum. Accordingly, λ in the model (1) is measured in units of $m^2\omega^3/\hbar$. The quantum dynamics is governed by the evolution operator $U(t) = \exp[-iHt/\hbar]$. The connection between quantum and classical domains is done by the preparation of the initial coherent state $|\psi(0)\rangle = |\alpha_1\rangle \otimes |\alpha_2\rangle$, whose center is precisely on a classical phase space point $(q_1, p_1; q_2, p_2)$ with $\alpha_l = (q_l + ip_l)/\sqrt{2}(l=1,2)$ [19]. In the natural units, the state $|\alpha_l\rangle$ is a minimum uncertainty packet centered on a phase point with a width $O(1)$ in both the length and momentum directions. Besides, the entanglement is quantified by von Neumann entropy S_V [20].
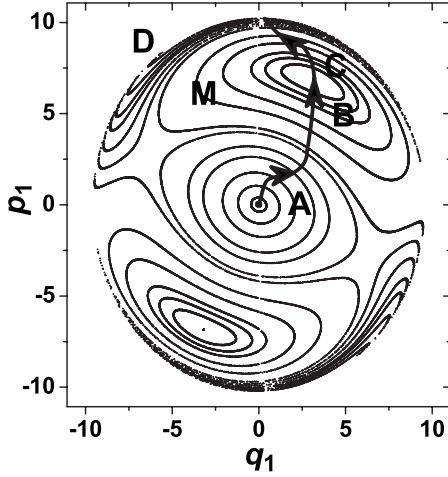
FIG. 1. Poincaré section ($q_2=\sqrt{10}$ and $p_2>0$) for the regular case. The three regular islands are marked along the arrow line with **A**, **M**, and **D**. **B**(**C**) denotes the upper (lower) half part of **M**. Unit of q_1 is $\sqrt{\hbar/m\omega}$, and that of p_1 is $\sqrt{\hbar m\omega}$.

A. Entanglement production in the regular case

The classical dynamics of model (1) exhibits a regular phase space with $\lambda=0.0075$ and total energy $E=58$ (in the natural units). In the classical phase space, we choose 21 classical trajectories to explore the connections between entanglement production and classical dynamics. The Poincaré section of these trajectories is shown in Fig. 1. The three regular islands are marked with **A**, **M**, and **D**. **B** (**C**) denotes the upper (lower) half part of the island **M**. In each regular island, there are seven tori.

From the tori in the island **A**, **M**, and **D**, we pick up the centers of the initial coherent states (CICS) along an arrow line. As shown in Fig. 1, the arrow line starts from the origin in **A**, passes through the innermost torus in **M**, and then reaches the minimum torus in **D**. Between the arrow line and the tori in **A**, **B**, **C**, and **D**, there are 27 cross points. We pick up these cross points along the arrow line and display their coordinates in Table I in turn (p_2 are determined by energy conservation and thus are not shown hereafter). The rows A, B, C, and D display the coordinates of the cross points sampled from the tori in **A**, **B**, **C**, and **D**, respectively. For

TABLE I. Coordinates of the CICS sampled from the tori in Fig. 1.

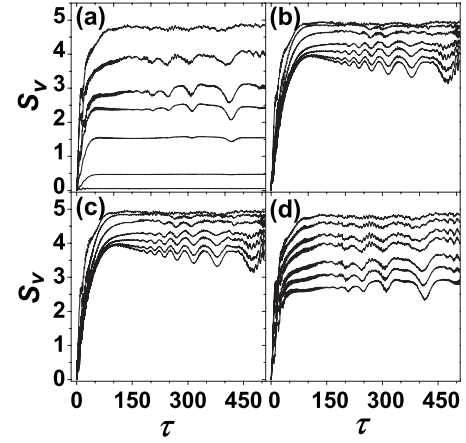| Regions	$(q_1/\sqrt{10},p_1/\sqrt{10})$ with fixed $q_2=\sqrt{10}$ and $p_2>0$
A	(0,0), (0,0.121), (2/9,0.242), (4/9,0.36), (1,0), (1,0.458), (1,0.801);
B	(0.74,1.08), (0.9,1.31), (0.92,1.53), (0.96,1.74), (0.98,1.84), (1,1.95), (1,2.173);
C	(1,2.173), (0.9,2.4072), (0.8,2.5234), (0.6266,2.631), (0.33,2.8016), (0.245,2.933), (0.126,3.0748);
D	(0.1,3.11), (0.07,3.14), (0.06,3.17), (0.04,3.187), (0.02,3.21), (0.01,3.2,32), (0,3.25576)

FIG. 2. von Neumann entropy S_V vs time $\tau=\omega t$ for different initial states (see Table I). The CICS for the entropy curves in (a), (b), (c), and (d) are localized on the tori in **A**, **B**, **C**, and **D** (see Fig. 1), respectively. Unit of τ is ω^{-1}.

comparison purpose, the nodal coordinates taken from the innermost torus in **M** are shown in both the rows B and C with $(q_1,p_1)=(\sqrt{10},2.173\sqrt{10})$.

The cross points chosen above are used as the CICS in the quantum evolution. With $E=58$, the distance between any two adjacent cross points is approximately equal to 1 in the units used in this section. As mentioned above, the scales of the initial states in the same units are $O(1)$ in both the length and momentum directions. Thus, the distance between any two adjacent CICS is approximately equal to the scales of the initial states. This makes sure that we are treating a semiclassical regime.

With the CICS chosen above, we calculate the von Neumann entropies $S_V(t)$ and show the results in Fig. 2. The entropy curves in Fig. 2(a) [Fig. 2(c)] from bottom to top correspond to the CICS in the row A (C) of Table I from first to last, while those in Fig. 2(b) [Fig. 2(d)] from top to bottom correspondent to the CICS in the row B (D) from first to last. Accordingly, the entropy curves in Figs. 2(a)–2(d) correspond to the tori in **A**, **B**, **C**, and **D** in Fig. 1, respectively. Especially, as the tori in **A**, **B**, **C**, and **D** enlarge from the innermost to the outermost, the entropy curves in the corresponding subfigure of Fig. 2 increase from bottom to top.

To clarify the dependence of entanglement production on classical trajectories, we further calculate the maximum values of the entropy curves in Fig. 2 and show the results (i.e., the maximum von Neumann entropies) in Fig. 3. The maximum entropies S_M in Fig. 3 are arranged in the same order as their corresponding CICS are picked up from the tori along the arrow line in Fig. 1 (i.e., the CICS of the kth S_M in Fig. 3 correspond to the kth cross point picked up from the tori along the arrow line in Fig. 1).

In Fig. 3, the maximum von Neumann entropies S_M vary significantly with the corresponding classical invariant tori. For instance, as the tori in the island **A** enlarge from the innermost to the outermost, the corresponding S_M's in Fig. 3 increase from the first square to the seventh square. Then, as the tori in **B** shrink from the outermost to the innermost, the values of S_M in Fig. 3 decrease from the first diamond to the
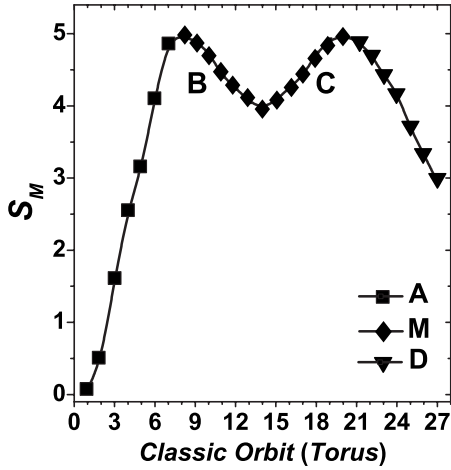
FIG. 3. Maximum von Neumann entropy S_M vs corresponding classical trajectory. The squares, diamonds and triangles denotes the S_M's corresponding to the tori in **A**, **M**, and **D** (see Fig. 1), respectively.

valley between "B" and "C." For the CICS localized on the tori in **C** and **D**, the curve of S_M also varies with the classical tori in a similar way. Roughly speaking, the value of S_M increases (decreases) with the enlargement (shrink) of the classical tori and is maximized when the corresponding torus lies at the edge of the regular islands. Furthermore, since different entropy curves in Fig. 2 reach the saturation plateaus almost at the same time, a larger S_M indicates a faster generation of entanglement. Thus, the rate of entanglement production also roughly increases (decreases) with the enlargement (shrink) of the classical tori.

Besides, in the investigations, we also note that there is good correspondence between the oscillations of the entropy $S_V(t)$ and those of the underlying classical coupling potential $\lambda q_1^2(t) q_2^2(t)$ for some classical trajectories. The oscillations of classical coupling potential reveal the frequency distribution of classical trajectory. We thus perform frequency analyses of the classical trajectories and further find interesting connections between the entanglement production and the classical power spectrum.

Classical power spectrum is used to analyze the frequencies of classical motion [21]. For a classical trajectory, the classical motion is generally multiply periodic, admitting the Fourier expansion [22]

$$\mathbf{x}(t) = \sum_{\mathbf{m}} \mathbf{X_m}(\mathbf{I}) \exp[i\mathbf{m} \cdot (\boldsymbol{\omega} t + \boldsymbol{\theta}_0)], \quad (2)$$

where $\mathbf{x}(t)$ stands for some dynamical variable such as position coordinate $\mathbf{q}(t)$, and $\boldsymbol{\omega}$ are the frequencies related to the actions $\mathbf{I}$. The integer set $\mathbf{m}(m_1, m_2)$ goes from $-\infty$ to $+\infty$ and the coefficients $\mathbf{X_m}(\mathbf{I})$ are dependent on $\mathbf{I}$. With the Fourier expansion (2), the frequencies of a classical trajectory can be obtained using a numerical integration [22]

$$I_\alpha(\omega') = \frac{1}{2\pi} \lim_{T \to \infty} \frac{1}{T} \left| \int_0^T dt \, x_\alpha(t) \exp(-i\omega't) \right|^2, \quad (3)$$

where $x_\alpha(t)$ denotes the αth component of $\mathbf{x}(t)$. Specifically, for the αth component of $\mathbf{q}(t)$ $(\alpha = 1, 2)$, $q_\alpha(t)$
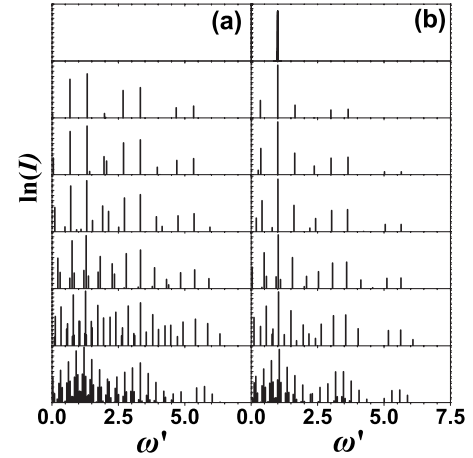

FIG. 4. Power spectra of (a) q_1 and (b) q_2 for the trajectories whose tori lie in the island **A** (see Fig. 1). The seven pairs of spectra from top to bottom correspond to the seven tori in **A** from the innermost to the outermost. Unit of ω' is ω.

$= \sum_{\mathbf{m}} Q_{\mathbf{m}}^\alpha(\mathbf{I}) \exp[i\mathbf{m} \cdot (\boldsymbol{\omega} t + \boldsymbol{\theta}_0)]$ and the power spectrum becomes $I_\alpha(\omega') = \sum_{\mathbf{m}} |Q_{\mathbf{m}}^\alpha|^2 \delta(\omega' - \mathbf{m} \cdot \boldsymbol{\omega})$.

With the EBK method shown in Ref. [21], we calculate the classical power spectra of $q_\alpha(t)(\alpha = 1, 2)$ for the 21 classical trajectories chosen above (the evolution time $\tau = \omega t = 2^{17}$). Figures 4 and 5 display the results for the trajectories whose tori lie in **A** and **B** (see Fig. 1), respectively. The results for the tori in **D** (**C**) are similar to those for the tori in **A** (**B**) and thus are not shown here. For comparison purpose, the strength axis in the power spectrum is plotted in logarithmic scale (i.e., $\ln[I(\omega')]$ hereafter).

The seven pairs of power spectra in Fig. 4 from top to bottom correspond to the seven entropy curves in Fig. 2(a) from bottom to top, while those in Fig. 5 from top to bottom correspond to the seven $S_V(t)$ curves in Fig. 2(b) from bottom to top. It is clear that more complicated power spectra correspond to higher maximum values and faster rates of en-
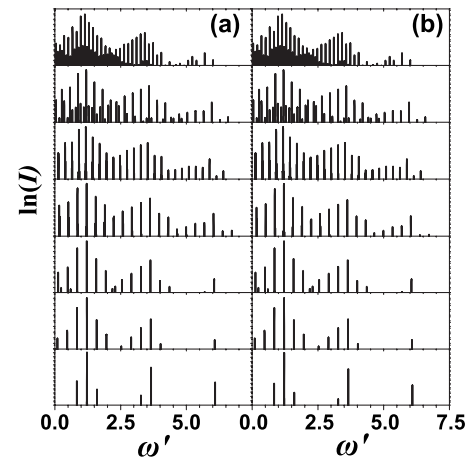

FIG. 5. As in Fig. 4 but for the trajectories whose tori lie in the island **M** (see Fig. 1). The seven pairs of spectra from top to bottom correspond to the seven tori in **B** or **C** from the innermost to the outermost. Unit of ω' is ω.
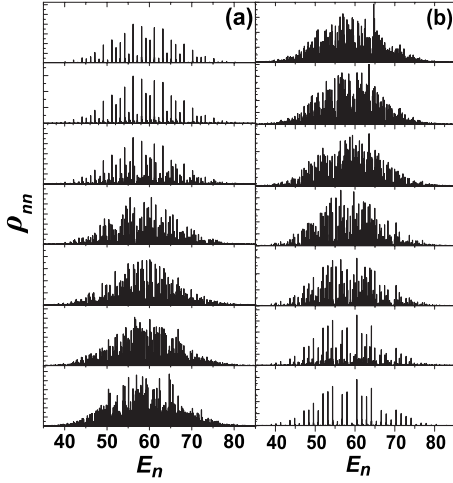
FIG. 6. Density spectrum $\{\rho_{nn}\}$ vs corresponding eigenenergy E_n. The spectra in the column (a) [(b)] from top to bottom correspond to the CICS in the row A (B) of Table I from first to last. Unit of E_n is $\hbar\omega$.
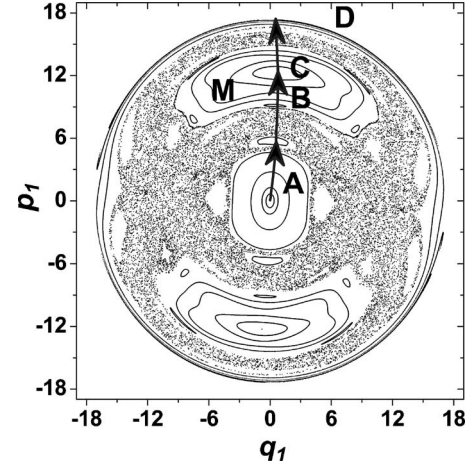

FIG. 7. Poincaré section ($q_2=\sqrt{5}$ and $p_2>0$) for the classical trajectories chosen in the mixed case. The three islands are marked along the arrow line with **A**, **M**, and **D**. **B** (**C**) denotes the upper (lower) half part of **M**. Unit of q_1 is $\sqrt{\hbar/m\omega}$, and that of p_1 is $\sqrt{\hbar m\omega}$.

tanglement production. Such correspondence is also found in the investigations related to the tori in **C** and **D** in Fig. 1.

In the spectra in Figs. 4 and 5, there are sharp lines at the frequencies ω'. Each line corresponds to a transition from one energy level to another. Its strength is related to a physical process, which involves the motion of the two particles [22]. Thus, classical power spectrum indicates the energy levels involved in the corresponding quantum evolution. The latter can be revealed by quantum density spectrum.

Quantum density spectrum is expressed as $\rho_{nn} = \langle n|\rho(t)|n\rangle$ [13], where $\rho(t)$ is the quantum density at time t and $|n\rangle$ are the eigenvectors of the Hamiltonian with E_n as the corresponding eigenvalues. According to Ghose *et al.* [13], a larger set of $\{\rho_{nn}\}$ correspond to a faster generation of entanglement in the regular to chaotic transition. Figures 6(a) and 6(b) display the quantum density spectra for the CICS localized on the tori in **A** and **B**, respectively. The seven spectra in Fig. 6(a) from top to bottom correspond to the seven pairs of classical power spectra in Fig. 4 from top to bottom. The same correspondence also holds between the quantum density spectra in Fig. 6(b) and the classical power spectra in Fig. 5. From the above comparisons, we can see that more complicated classical power spectrum corresponds to larger set of $\{\rho_{nn}\}$. Since $\{\rho_{nn}\}$ is closely related to quantum entropy [13], the correspondence between the classical power spectrum and the quantum density spectrum indicates the connections between the entanglement production and the classical trajectories.

B. Entanglement production in the mixed case

With $\lambda=0.0075$ and $E=150.75$ (in units of $\hbar\omega$), the classical dynamics of the Hamiltonian (1) exhibits a mixed phase space. In the classical phase space, we choose 17 regular classical trajectories and four chaotic ones, and show their Poincaré section in Fig. 7. The three islands formed by the regular trajectories are marked along the arrow line with **A**,

M, and **D**. **B**(**C**) denotes the lower (half) part of the island **M**. In each regular island, there are six tori.

Between the arrow line and the tori in **A**, **M**, and **D**, there are 23 cross points. These cross points are used as the CICS in the quantum evolution. Along the direction of the arrow line in Fig. 7, we pick up these cross points and present their coordinates in turn in the lower four rows of Table II. Specifically, the rows A, B, C, and D show the CICS sampled from the tori in **A**, **B**, **C**, and **D** (see Fig. 7), respectively. For comparison purpose, the coordinates of the CICS sampled from the innermost torus in $\underline{M}$ are shown in both the rows B and C with $(q_1,p_1)=(\sqrt{10}/4, 3.8737\sqrt{10})$. Besides, we sample four CICS from the chaotic sea and display their coordinates in the first row of Table II. Similar to the regular case, with $E=150.75$ (in units of $\hbar\omega$), the distance between any two CICS in Table II is also approximately equal to or larger than the length and momentum scales of the initial states. In addition, the initial states corresponding to the chaotic CICS are fully contained in the chaotic sea.

We calculate the von Neumann entropies for the CICS in Table II, and present the results in Fig. 8. The topmost en-

TABLE II. Coordinates of the chaotic CICS and those of the regular CICS sampled from the tori in Fig. 7.

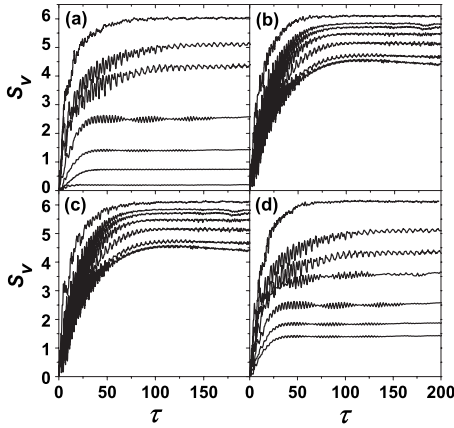| Regions	$(q_1/\sqrt{10}, p_1/\sqrt{10})$ with fixed $q_2=\sqrt{5}$ and $p_2>0$
Chaotic sea	(1/4,2.2427), (−2.3963,1.3352), (−2.0246, −1.1064), (1/4,4.4846);
A	(0,0), (1/36,0.2041), (1/4,0), (1/4,0.7155), (1/4,1.5050), (1/4,1.9102);
B	(1/4,2.9143), (1/4,3.0582), (1/4,3.2621), (1/4,3.4660), (1/4,3.6699), (1/4,3.8737);
C	(1/4,3.8737), (1/4,4.0690), (1/4,4.2440), (1/4,4.4026), (1/4,4.5466), (1/4,4.6402);
D	(1/4, 5.1357), (1/4,5.2687), (1/4,5.3412), (1/4,5.4184), (1/4,5.4643), (1/4,5.4795).

FIG. 8. von Neumann entropy S_V vs time $\tau = \omega t$ for the CICS on different classical trajectories (see Table II). The topmost curves in (a) to (d) correspond to the four chaotic CICS. The others in (a), (b), (c), and (d) correspond to the CICS on the tori in **A**, **B**, **C**, and **D**, respectively. Unit of τ is ω^{-1}.

tropy curves in Figs. 8(a) to 8(d) correspond to the four chaotic CICS in Table II from first to last. The lower six entropy curves in Fig. 8(a) [Fig. 8(c)] from bottom to top correspond to the six CICS in the row A (B) of Table II from first to last, while the lower six entropy curves in Fig. 8(b) [Fig. 8(d)] from top to bottom correspond to the six CICS in the row B (D) of Table II from first to last.

We further calculate the maximum values S_M of the entropy curves in Fig. 8 and display the results in Fig. 9. The four S_M's marked with circles from first to last correspond to the four chaotic CICS in Table II from first to last. The S_M's marked with squares, diamonds, and triangles correspond to the regular CICS localized on the tori in the island **A**, **M**, and **D**, respectively. Similar to the regular case, the S_M's obtained with the regular CICS are arranged in Fig. 9 in the same order as their corresponding CICS are sampled from the tori along the arrow line in Fig. 7. For instance, the CICS of the
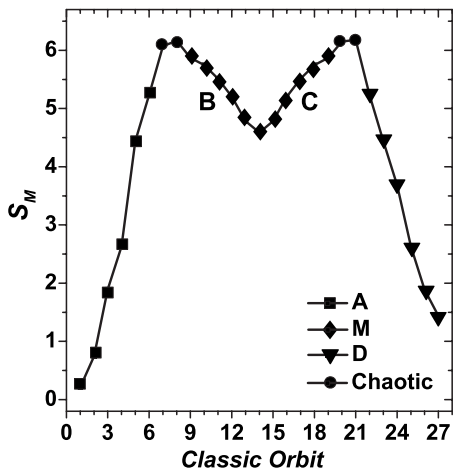

FIG. 9. Maximum von Neumann entropy S_M vs corresponding classical trajectory. The circles correspond to the chaotic trajectories. The squares, diamonds and triangles correspond to the tori in **A**, **M**, and **D**, respectively.
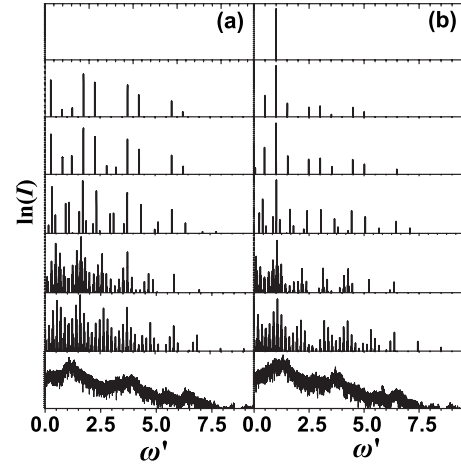

FIG. 10. Power spectra of (a) q_1 and (b) q_2 for different classical trajectories. The upper six pairs from top to bottom correspond to the six tori in **A** (Fig. 7) from the innermost to the outermost. The bottom pair corresponds to a chaotic trajectory. Unit of ω' is ω.

S_M's numbered from one to six in Fig. 9 are sampled from the six tori in **A** from the innermost to the outermost. In Fig. 9, the curve of S_M varies with the classical tori and is maximized when the CICS lies in the chaotic sea. So do the growth rates of the entropy curves as shown in Fig. 8.

We investigate the power spectra of all the above classical trajectories with the EBK methods (the evolution time $\tau = 2^{17}$) [21]. In Fig. 10, we exhibit the results for the six tori in the island **A** and those for a chaotic trajectory with $(q_1, p_1) = (\sqrt{10}/4, 2.2427\sqrt{10})$ (see Table II) as initial conditions. The upper six pairs of spectra in Fig. 10 from top to bottom correspond to the six tori in the island **A** from the innermost to the outermost. Also they correspond, from top to bottom, to the lower six entropy curves in Fig. 8(a) from bottom to top. The bottom pair is the power spectra of the chaotic trajectory and corresponds to the top entropy curve in Fig. 8(a). A comparison between Figs. 10 and 8(a) shows that more complicated power spectra correspond to larger and faster entanglement production. Such correspondence is also found in the investigations on the relation between the entanglement production and the classical power spectra for the other classical trajectories. Especially, when the trajectory is chaotic, the power spectrum is continuous and the corresponding entanglement production is maximized.

In Fig. 8, there are relatively small differences in both the maximum values and the growth rates between the four chaotic entropy curves. This is because the instabilities of the chaotic trajectories are similar to each other, for the chaotic power spectra are all continuous and the Lyapunov exponents of the four chaotic trajectories are around 0.12 ± 0.02. This is in accord with the previous suggestion [3,9,23] that the enhancement of entanglement production induced by chaos depends on the Lyapunov exponent.

A comparison of Figs. 3 and 9 shows that the curve of S_M in Fig. 3 is similar to that in Fig. 9, though the classical dynamics transits from the regular case to the mixed case. Especially, the variation of S_M in Fig. 9 through the transition to the chaotic trajectories is similar to that in Fig. 3 through
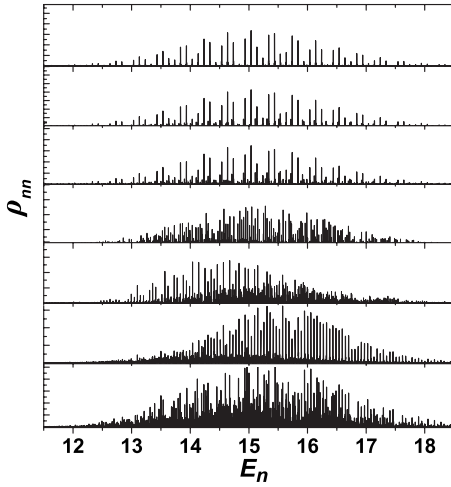
FIG. 11. Density spectra $\{\rho_{nn}\}$ vs corresponding eigenenergy E_n. The upper six spectra from top to bottom correspond to the six CICS in the row A of Table II from fist to last. The bottom one correspond to the CICS localized in the chaotic sea with $(q_1, p_1) = (\sqrt{10}/4, 2.2427\sqrt{10})$. Unit of E_n is $\hbar\omega$.

the transition to the edges of the regular islands. This suggests that entanglement production is an indicator not only of the regular to chaotic transition but also of the transitions in different regular classical trajectories.

To further investigate the quantum-classical correspondence in entanglement production, we calculate the quantum density spectra corresponding to the CICS shown in Table II. In Fig. 11, we exhibit the results for the CICS shown in the row A of Table II and those for a chaotic CICS with $(q_1, p_1) = (\sqrt{10}/4, 2.2427\sqrt{10})$. The seven density spectra in Fig. 11 from top to bottom correspond to the seven entropy curves in Fig. 8(a) from bottom to top. Also they correspond, from top to bottom, to the classical power spectra in Fig. 10 from top to bottom. Similar to the regular case, a comparison of Figs. 10 and 11 indicates that a larger set of frequency components involved in the classical dymanics corresponds to larger set of eigenstates involved in the quantum evolution.

C. Frequency entropy and quantum-classical correspondence

In the above investigations on the coupled oscillators, we show that entanglement production depends systematically on classical invariant tori. When the initial state lies at the edge of regular islands for the regular case or in the chaotic sea for the mixed case, the entanglement production is maximized. As shown in the previous studies [3,9,23], the enhancement of entanglement production induced by chaos has been investigated and explained by the methods related to the Lyapunov exponents.

Here we further develop a practical method to describe the dependence of entanglement production on classical tori from the perspective of classical power spectra. We use $I_k^\alpha(\omega')$ to stand for the amplitude of the kth component in the discrete power spectrum of $q_\alpha(\alpha=1,2)$. To describe the discrete classical spectral distribution, we consider a new quantity as

$$J_k^\alpha(\omega') = I_k^\alpha(\omega') \bigg/ \sum_{\alpha,k} I_k^\alpha(\omega'). \qquad (4)$$

We then define a frequency entropy S_{fr} as a measure of the classical frequencies, i.e.,

$$S_{\text{fr}} = -\sum_{\alpha,k} J_k^\alpha(\omega)\ln J_k^\alpha(\omega'), \qquad (5)$$

which is used to distinguish different regular trajectories and measure the stability of classical dynamics.

With the above method, we investigate the classical frequency entropies of all the regular trajectories chosen in the regular and mixed cases. The results are presented in Fig. 12. The classical frequency entropies S_{fr} and the corresponding maximum von Neumann entropies S_M are represented by squares and circles, respectively. The S_M's are shown in the same way in Fig. 12(a) [Fig. 12(b)] as they are shown in Fig. 3 (Fig. 9). In Figs. 12(a) and 12(b), there is good correspondence between the variations of S_M and S_{fr} with the classical trajectories. This clearly indicates the quantum-classical correspondence in the production of entanglement.

For the continuous power spectrum of chaotic trajectories, the summation over k in Eqs. (4) and (5) is replaced by the integral over the frequency ω'. Using this method, we can obtain the frequency entropies of classical chaotic trajectories. However, due to the continuity of chaotic power spectrum, the classical frequency entropies of chaotic trajectories are not consistent with those of regular trajectories. Further research will be needed to study the classical frequency entropies of chaotic trajectories. It is conceivable, however, that
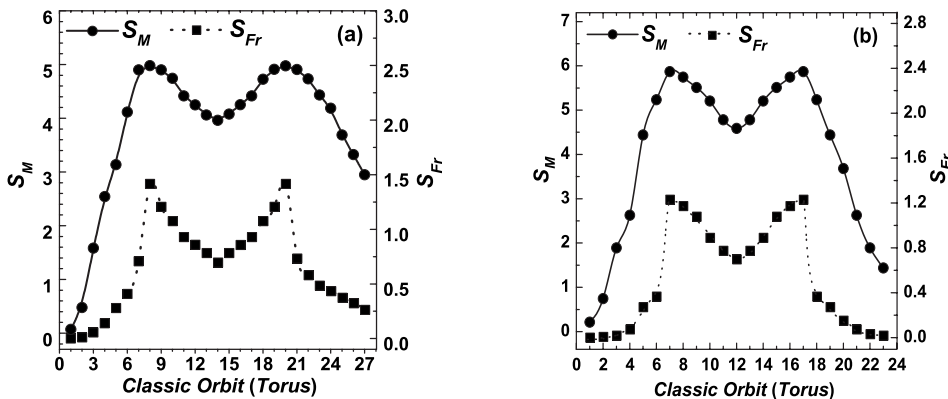

FIG. 12. Maximum von Neumann entropy S_M (solid) and classical frequency entropy S_{Fr} (dotted) vs corresponding regular trajectory in (a) the regular case ($E=58$) and (b) the mixed case ($E=150.75$).

in Fig. 9 the S_M's corresponding to the chaotic trajectories are larger than those corresponding to the regular trajectories, for the chaotic power spectra are continuous and have more frequency components.

As mentioned above, the enhancement of entanglement induced by chaos has been discussed and explained by the methods related to the Lyapunov exponent. Here, to further understand the connections between the production of entanglement and the power spectrum of regular classical trajectories, we can get some clews from a general method of quantum-classical correspondence presented by Brumer *et al.* based on the Liouville mechanics [10–12]. Following this method, the time evolution of a classical property $\mathbf{x}(t)$ can be expressed as [10,12]

$$\mathbf{x}(t) = \text{tr}[\rho(t)\mathbf{x}] = \sum_{\lambda,\alpha} \mathbf{X}_{\lambda,\alpha} \exp[-i\lambda t], \qquad (6)$$

where $\mathbf{x}(t)$ denotes some dynamical variable [e.g., position coordinate $\mathbf{q}(t)$] and $\rho(t)$ is the classical density function. The coefficient $\mathbf{X}_{\lambda,\alpha}$ depends on the initial conditions. The parameter λ is the classical correspondence of $\lambda_{\mathbf{nm}} = (E_{\mathbf{m}} - E_{\mathbf{n}})/\hbar$ [12], where $E_{\mathbf{n}}(E_{\mathbf{m}})$ is the eigenvalue of the Hamiltonian with $|\mathbf{n}\rangle(|\mathbf{m}\rangle)$ as the corresponding eigenstate. The label α is the degeneracy related to λ [12].

For regular motion, $\lambda = \mathbf{k} \cdot \boldsymbol{\omega}(\mathbf{I}')$ [12], where each member of the integer set $\mathbf{k}$ goes from $-\infty$ to $+\infty$ and $\boldsymbol{\omega}(\mathbf{I}')$ is the frequency dependent on the action $\mathbf{I}'$. By comparing Eq. (6) with Eq. (2), one can see that the set of frequencies $\{\omega' = \mathbf{m} \cdot \boldsymbol{\omega}\}$ in Eq. (2) are equivalent to $\{\lambda = \mathbf{k} \cdot \boldsymbol{\omega}(\mathbf{I}')\}$ in Eq. (6) (each member of the integer set $\mathbf{m}$ also goes from $-\infty$ to $+\infty$). Since $\lambda = \mathbf{k} \cdot \boldsymbol{\omega}(\mathbf{I}')$ corresponds to $\lambda_{\mathbf{nm}} = (E_{\mathbf{m}} - E_{\mathbf{n}})/\hbar$ in the quantum counterpart, the frequency lines at $\omega' = \mathbf{m} \cdot \boldsymbol{\omega}$ in the classical power spectrum reveal the structure of the energy levels involved in the quantum evolution. More complicated classical power spectrum indicates larger set of eigenstates extending over broader and denser quantum density spectrum (the latter can enhance the entanglement production [13]). Such connection is also revealed in the comparisons between the classical power spectra and the quantum density spectra shown in the first two parts of this section. Similar to the Lyapunov exponent, the classical power spectrum and the classical frequency entropy suggest a simple method to indicate the dependence of entanglement on classical dynamics.

III. ENTANGLEMENT PRODUCTION OF THE JAYNES-CUMMINGS MODEL

To confirm the connection between the entanglement and the classical frequency entropy, we perform similar investigations on the Jaynes-Cummings model. The Hamiltonian reads [2]

$$H = \hbar\omega a^\dagger a + \varepsilon J_z + \frac{G}{\sqrt{2J}}(aJ_+ + a^\dagger J_-) + \frac{G'}{\sqrt{2J}}(a^\dagger J_+ + aJ_-),$$

$$(7)$$

where the first term corresponds to the free single-mode field with frequency ω, the second term corresponds to the N
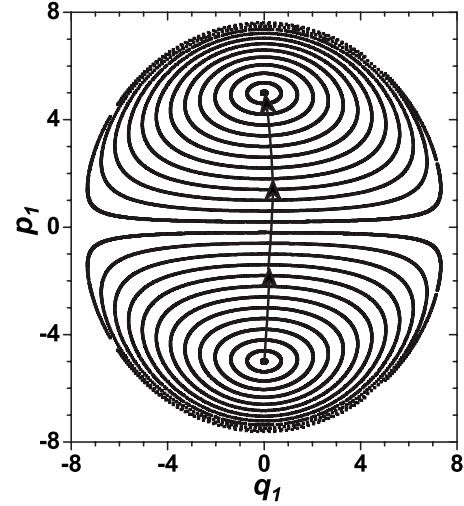

FIG. 13. Poincaré section ($q_2=0$, $p_2>0$) for the Jaynes-Cummings model with $E=40$, $J/2=14.5$, $G=0.25$, and $G'=0$. q_1 and p_1 are given in the natural units.

$=2J$ two-level atoms with energy separation $\hbar\varepsilon$, and the other terms are the interaction between the field and the atoms. Here, we set $\omega=\varepsilon=1$ and use the natural units, i.e., $\hbar=c=1$.

The connection between the classical and quantum domains is done by the choice of the initial states. Given a point $(q_1,p_1;q_2,p_2)$ in the classical phase space, the corresponding quantum initial state is $|\psi(0)\rangle = |w\rangle \otimes |v\rangle$. $|w\rangle(|v\rangle)$ are the atomic (field)-coherent states given by $|w\rangle = (1+w\bar{w})^{-J}e^{wJ_+}|J,-J\rangle$ and $|v\rangle = e^{-w\bar{w}/2}e^{va^\dagger}|0\rangle$ with $w=(p_1+iq_1)/\sqrt{4J-(p_1^2+q_1^2)}$ and $v=(p_2+iq_2)/\sqrt{2}$ [24].

The classical version of the Hamiltonian (7) is obtained by a procedure as $H(v,v^*;w,w^*) \equiv \langle wv|H|wv\rangle$. It can be rewritten in terms of the phase-space variables as [25]

$$H(q_1,p_1;q_2,p_2) = \frac{\omega}{2}(q_2^2 + p_2^2) + \frac{\varepsilon}{2}(q_1^2 + p_1^2 - 2J)$$

$$+ \sqrt{1 - \frac{(q_1^2 + p_1^2)}{4J}}(G_+p_1p_2 + G_-q_1q_2),$$

$$(8)$$

where $G_\pm = G \pm G'$.

Using the model (7), we investigate the connections between the von Neumann entropies and the frequency entropies for different classical trajectories in both regular and mixed cases. In the calculations, the evolution time for calculating S_M is approximately equal to 350; and that for calculating S_{fr} is approximately equal to 5×10^5 (in the natural units).

The Poincaré section in Fig. 13 exhibits a regular phase space of the model (8) with $E=40$. As shown in Fig. 13, we pick up 15 CICS along the arrow line from different tori and present their coordinates (q_1,p_1) in turn as follows: (0.1, -5.005), (0.1, -4.6046), (0.1, -4.2042), (0.1, -3.8038), (0.1, -3.4034), (0.1, -2.6026), (0.1, -1.8018), and (0.1,
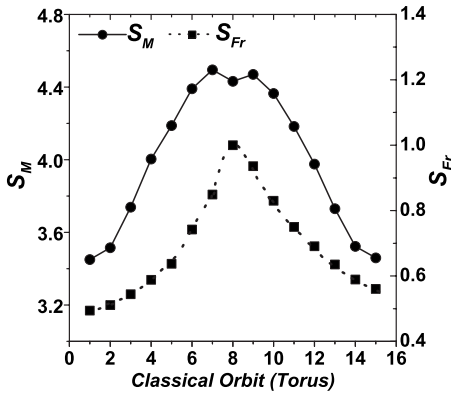
FIG. 14. Maximum von Neumann entropy S_M (solid) and classical frequency entropy S_{Fr} (dotted) vs corresponding torus (see Fig. 13).

−0.6006), from tori in the lower island; $(0.1, 1.8018)$, $(0.1, 2.6026)$, $(0.1, 3.1534)$, $(0.1, 3.5538)$, $(0.1, 4.9542)$, $(0.1, 4.3546)$, and $(0.1, 5.005)$, from the tori in the upper island. For all the CICS in this section, $q_2 = 0$, $p_2 > 0$ and the values of p_2 are determined by energy conservation.

Figure 14 shows the maximum von Neumann entropies S_M (solid line) for the above 15 CICS and their corresponding classical frequency entropies S_{Fr} (dotted line). In Fig. 14, the S_M's numbered from one to 15 correspond to the above 15 CICS from first to last. As shown in Fig. 14, the curves of S_M and S_{fr} vary significantly with the underlying classical trajectories. Furthermore, their variations with the classical tori are synchronous.

Figure 15 shows the Poincaré section of the classical Hamiltonian (8) in a mixed case. We sample the CICS from different classical trajectories along the arrow line and show their coordinates (q_1, p_1) in turn as follows: $(0.1, -5.86)$, $(0.1, -5.0792)$, $(0.1, -4.27)$, and $(0.1, -3.4521)$, from the tori in the island **A**; $(2.21, -2.2924)$ and $(2.424, -3.078)$, from
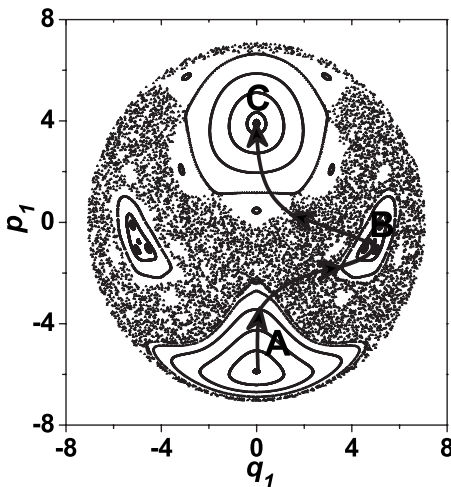

FIG. 15. Poincaré section ($q_2 = 0$ and $p_2 > 0$) for the Jaynes-Cummings model with $E = 35$, $J/2 = 12.5$, $G = 0.4$, and $G' = 0.25$. The three islands are marked along the arrow line with **A**, **B**, and **C**. Units are as in Fig. 13.
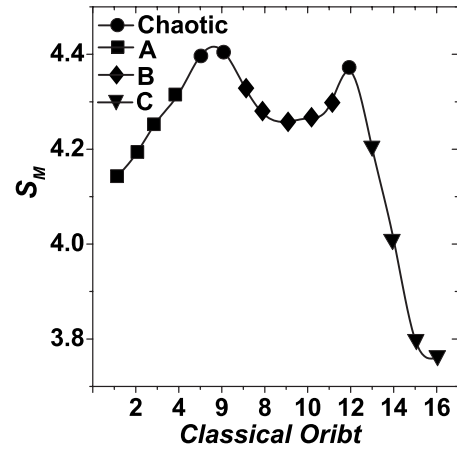

FIG. 16. Maximum von Neumann entropy S_M vs corresponding classical trajectory. The circles correspond to the chaotic trajectories. The squares, diamonds, and triangles correspond to the tori in **A**, **B**, and **C**, respectively.

the chaotic sea; $(4.21, -2.19)$, $(4.9, -1.46)$, $(4.9, -0.8)$, $(4.7471, -0.4992)$, and $(4.7295, 0.13558)$, from the tori in the island **B**; $(2.2302, -0.66822)$, from the chaotic sea; $(1.71259, 2.6883)$, $(1.0029, 3.2417)$, $(0.1, 3.5096)$, and $(0.1, 3.9)$, from the tori in the island **C**.

We calculate the maximum von Neumann entropies S_M for the above 16 CICS and show the results in Fig. 16. Here, the S_M's from first to last correspond to the above 16 CICS from first to last. The curve of S_M in Fig. 16 exhibits the variation of the maximum entanglement with the underlying classical trajectories. Among these classical trajectories, there are 13 regular ones, whose tori lie in the island **A**, **B**, and **C** (see Fig. 15). Figure 17 displays the classical frequency entropies for these regular classical trajectories. In Fig. 17, the squares and circles stand for the classical frequency entropies and their corresponding maximum von Neumann entropies, respectively. From Fig. 17, one also can see that there is good correspondence between the maximum von Neumann entropies and the classical frequency entropies.
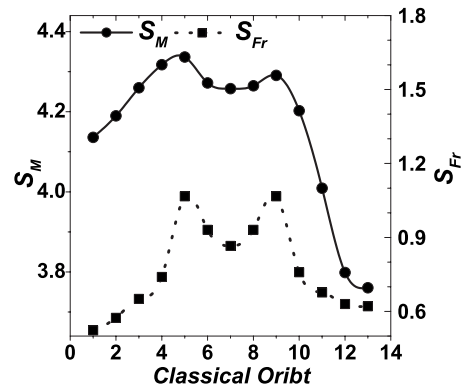

FIG. 17. Maximum von Neumann entropy S_M (solid) and classical frequency entropy S_{fr} (dotted) for the regular trajectories vs corresponding tori shown in Fig. 15.

IV. CONCLUSION

In this paper, using the model of coupled oscillators and the Jaynes-Cummings system, we show that the entanglement production of bipartite system changes systematically with classical invariant tori in both the regular and mixed cases. Furthermore, the dependence of entanglement on the underlying classical trajectories is closely related to the classical power spectrum. The larger the number of classical frequency components is, the larger the corresponding entanglement is. Such phenomena reveal the quantum-classical correspondence in the entanglement production from the perspective of classical trajectories. This sheds light on the further understanding of the quantum-classical correspondence in the entanglement production of chaotic systems.

[1] A. O. Bolivar, *Quantum-Classical Correspondence: Dynamical Quantization and the Classical Limit* (Springer, New York, 2004).

[2] K. Furuya, M. C. Nemes, and G. Q. Pellegrino, Phys. Rev. Lett. **80**, 5524 (1998).

[3] P. A. Miller and S. Sarkar, Phys. Rev. E **60**, 1542 (1999); A. Lakshminarayan, *ibid.* **64**, 036207 (2001).

[4] J. N. Bandyopadhyay and A. Lakshminarayan, Phys. Rev. Lett. **89**, 060402 (2002).

[5] A. Tanaka, H. Fujisaki, and T. Miyadera, Phys. Rev. E **66**, 045201(R) (2002); X. Wang, S. Ghose, B. C. Sanders, and B. Hu, *ibid.* **70**, 016217 (2004); A. Lahiri and S. Nag, Phys. Lett. A **318**, 6 (2003); A. J. Scott and C. M. Caves, J. Phys. A **36**, 9553 (2003).

[6] J. N. Bandyopadhyay and A. Lakshminarayan, Phys. Rev. E **69**, 016201 (2004).

[7] H. Fujisaki, T. Miyadera, and A. Tanaka, Phys. Rev. E **67**, 066201 (2003).

[8] M. Lombardi and A. Matzkin, Phys. Rev. A **73**, 062335 (2006).

[9] Ph. Jacquod, Phys. Rev. Lett. **92**, 150403 (2004).

[10] C. Jaffé and P. Brumer, J. Phys. Chem. **88**, 4829 (1984).

[11] C. Jaffé and P. Brumer, J. Chem. Phys. **82**, 2330 (1985).

[12] J. Wilkie and P. Brumer, Phys. Rev. A **55**, 27 (1997).

[13] S. Ghose and B. C. Sanders, Phys. Rev. A **70**, 062315 (2004).

[14] M. A. de Ponte, M. C. de Oliveira, and M. H. Y. Moussa, Ann. Phys. (N.Y.) **317**, 72 (2005).

[15] A. K. Rajagopal and R. W. Rendell, Phys. Rev. A **63**, 022116 (2001).

[16] D. Gottesman, A. Kitaev, and J. Preskill, Phys. Rev. A **64**, 012310 (2001); C. Hörhammer and H. Büttner, J. Phys. A **38**, 7325 (2005).

[17] R. A. Pullen and A. R. Edmonds, J. Phys. A **14**, L477 (1981).

[18] M. Feingold, N. Moiseyev, and A. Peres, Chem. Phys. Lett. **117**, 344 (1985); J. L. Anchell, J. Chem. Phys. **92**, 4342 (1990); Y. H. Zeng and R. A. Serota, Phys. Rev. B **50**, 2492 (1994); L. A. Caron, D. Huard, H. Kröger, G. Melkonyan, K. J. M. Moriarty, and L. P. Nadeau, J. Phys. Ai **37**, 6251 (2004); M. S. Santhanam, Phys. Rev. A **69**, 042301 (2004).

[19] M. Baranger, M. A. M. de Aguiar, F. Keck, H. J. Korsch, and B. Schellhaas, J. Phys. A **34**, 7227 (2001).

[20] C. H. Bennett, H. J. Bernstein, S. Popescu, and B. Schumacher, Phys. Rev. A **53**, 2046 (1996).

[21] D. W. Noid and R. A. Marcus, J. Chem. Phys. **67**, 559 (1977); Craig C. Martens and Gregory S. Ezra, *ibid.* **83**, 2990 (1985); D. W. Noid, M. L. Koszykowski, and R. A. Marcus, *ibid.* **73**, 391 (1980).

[22] M. C. Gutzwiller, *Chaos in Classical and Quantum Mechanics* (Springer, New York, 1990), p. 35.

[23] C. Petitjean and Ph. Jacquod, Phys. Rev. Lett. **97**, 194103 (2006).

[24] J. R. Klauber and B.-S. Skagertam, *Coherent States: Applications in Physics and Mathematical Physics* (World Scientific, Singapore, 1985).

[25] M. A. M. de Aguiar, K. Furuya, C. H. Lewenkopf, and M. C. Nemes, Ann. Phys. (N.Y.) **216**, 291 (1992).